ICESAR 2019 – A Study on Sea Ice based on F-SAR XCL-Band Data

Ralf Horn, Rolf Scheiber, Joel Amao-Oliva, Ronny Hänsch, Felix Weinmann, Marc Jäger
German Aerospace Center (DLR) e.V., Microwaves and Radar Institute, Oberpfaffenhofen, Germany

Abstract

This paper summarizes study results obtained about the characteristics of sea ice in the Davis Strait off the coast of Baffin Island in 2019. The study, also referred to as ICESAR 2019, is based on multi-frequency and interferometric data collected by the DLR F-SAR airborne radar in the course of the PermASAR campaign in the Canadian Arctic with the aim of improving knowledge on the radar properties of sea ice at different wavelengths and polarisations.

1 Introduction

Future SAR missions will operate with higher resolution, enhanced polarimetry modes and at a variety of frequency bands. In particular the STEREOID/HARMONY mission proposal consists of two bi-static passive synthetic aperture radar (SAR) receiver satellites to amend the next generation of ESA's C-band sensor. Its observations aim at improving estimations of sea ice roughness and thickness and support sea ice model development for improving operational forecast and mass balance studies to better understand the dynamics of sea ice [1].
In spring 2019 DLR's F-SAR sensor [2] was used to conduct a measurement flight east of Baffin Island with the purpose of studying the capability of ATI measurements to estimate sea ice drift and the value of a multi-mission constellation to classify sea ice characteristics by collecting X-, C- and L-band data.
This paper describes the measurement setup and the characteristics of the acquired data. First analyses are reported, demonstrating different methods for sea ice drift measurement and the potential for sea ice classification based on polarimetric SAR data.

2 The Baffin Island sea ice experiment

Towards the end of the PermASAR winter campaign in April 2019, the DLR airborne SAR team took the opportunity of conducting additional F-SAR data acquisitions over sea ice near Baffin Island, Nunavut province, Canada. The test flight was executed out of Iqaluit, also known as Frobisher Bay, on the return transfer from Yellowknife (Canada) to Oberpfaffenhofen (Germany). Observing the sea ice present in the Davis Strait by that time of year was of special interest to DLR to gain knowledge about polarimetric radar properties of sea ice at X-, C- and L-bands and to test the performance of the F-SAR X-band along-track interferometer (ATI) on drifting sea ice.

2.1 Experiment planning details

A 200km long transect was planned and flown on April 13, 2019, starting at a 200km distance from Frobisher Bay and heading out on a radial into a 60 to 150 degree sector to the east. Ice maps of Davis Strait provided by the Canadian Ice Service helped to narrow down the air operation area to a sector as shown in violet in **Figure 1**. Data were finally acquired on both out- and in-bound headings (90°/270°) with opposite look directions to the same area on the sea surface (red lines).

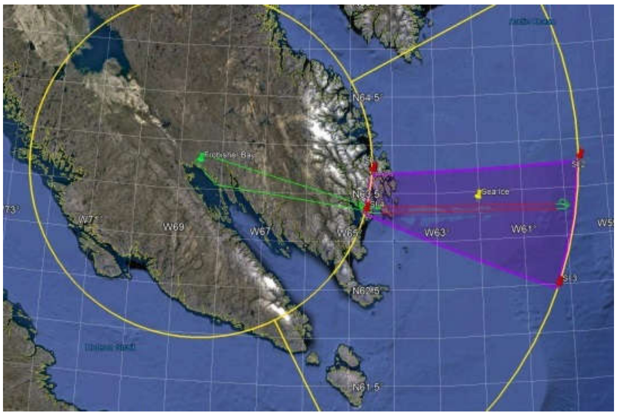

Figure 1 The sea ice transect off-coast Baffin Island. The F-SAR operation air space is indicated as a violet polygon. The F-SAR flight track out of Frobisher Bay is shown in green and red colours ('red' indicates where the radar measurements were performed).

Table 1: F-SAR technical parameters settings for IceSAR

Parameter	**X-band**	**C-band**	**L-band**
Center frequency [MHz]	9700	5300	1325
Bandwidth [MHz]	200	200	150
Flight altitude [m]	3036		
Incidence angles [deg]	25 – 55		
Channel PRF [Hz]	1202		
Azimuth resolution [m]	0.5	0.5	0.6
Slant range resolution [m]	1	1	1.3

Table 2: Acquisition details, flight dated 2019-04-13

ID	**Heading**	**Start time (GPS)**	**End time (GPS)**
19prmasr1702	90°	16:40:14.00	17:17:09.97
19prmasr1703	270°	17:29:15.00	18:06:08.41

3 Data processing & calibration

Dedicated calibration flights for the PermASAR campaign were performed at Yellowknife and included acquisitions in the along-track interferometric mode at X-band. These data were used to derive calibration corrections for the processing of SAR data gathered in the field. The Yellowknife calibration site featured three 2.5m trihedral radar reflectors deployed at off-nadir angles ranging from 30° to 50°. The responses of these reference targets were used as input to the calibration procedure described in [3], to obtain, among other things, precise antenna phase centre baselines for the X-band single-pass interferometers as well as calibration constants for the range delays, the channel gains and the inter-channel phase differences. In addition, the calibration included the estimation of a residual antenna phase error to correct for small phase inaccuracies in the on-ground characterisation of the antenna patterns. This estimate was carried out using phase differences measured over distributed targets in the range-Doppler domain to yield a 2D phase correction, in terms of off-nadir angle and squint, for the slave antenna of the X-band interferometer. The squint-variant estimate helped to ensure that the correction was transferrable to the imaging geometry of the IceSAR data acquisitions.

For SAR processing, the two stripes of SAR data were split into 20 overlapping segments, focused using the DLR's F-SAR processor and geocoded onto a 1m sampled reference UTM grid with heights corresponding to the EGM2008 geoid. For each segment, interferometric processing was performed to generate the along-track interferometric phases in X-band.

Figure 2 presents the X-band polarimetric RGB composites of 3 segments acquired during the outward overflight. They were selected to represent different ice drift regimes as obtained from the ATI phase. The further from the coast, the larger the ice flows become. For the five outer most segments (in the east), the sea ice cover becomes incomplete and reveals increasingly large areas of open water. The backscatter is dominated by surface reflection (represented in blue) in all frequency bands.

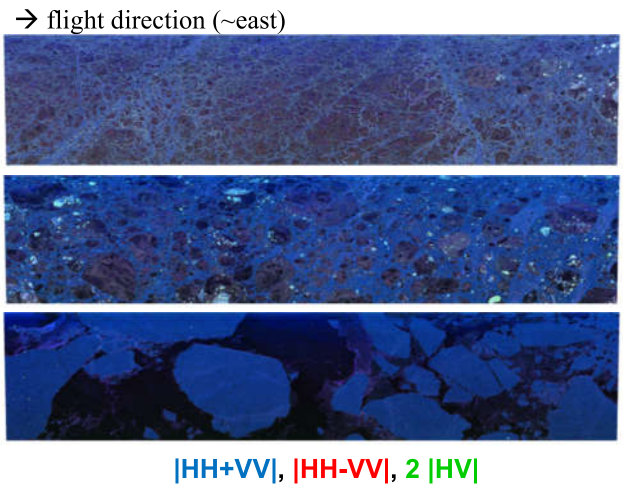

Figure 2 Polarimetric X-band SAR images in Pauli base, correponding to segments 3,5 and 18 of the outward flown pass.

4 Preliminary data evaluation

4.1 Sea ice drift estimates

The ICESAR 2019 data set offers several opportunities for estimating sea ice drift. Here we investigate the potential offered by ATI and by mutual shift estimates between geocoded data of outward and inward flown passes.

4.1.1 Along-track interferometry

Along track interferometry allows inferring radial ground velocity components v_{rad} from the interferometric phase ϕ_{if}:

$$v_{rad} = \frac{\lambda}{4\,\pi}\phi_{if}\frac{v_0}{B_{ATI}\cdot\sin(\theta_i)}\ , \qquad (1)$$

where λ is the wavelength, v_0 is the aircraft speed , B_{ATI} is the along track baseline, and θ_i is the incidence angle. The nominal unambiguous ground velocity range of the F-SAR configuration in full-baseline mode is +/- 2m/s.

Figure 3 presents the derived ice drift component (basically the north-south component) for the same segments of **Figure 2**. The segments were selected specifically to indicate the discontinuities in ice dynamics. The first segment shown (segment 3) reveals land fast ice in the western part (left) and velocities of around 0.5m/s in its eastern part (right). This is continued until segment 5, where there is a second discontinuity leading to velocity components of up to 1m/s. Finally, when reaching the open ocean, movement is still quite homogeneous but the velocity increases. In addition, small scale modulation effects overlay the large scale trend, which are attributed to the ice flow - ocean wave interaction.

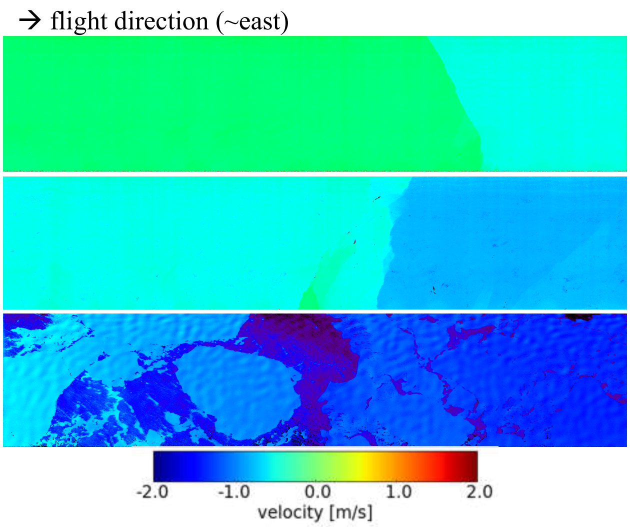

Figure 3 Radial ground velocity maps derived from X-band along-track interferometry, corresponding to segments 3,5 and 18 of the outward flown pass.

4.1.2 2D ice drift estimation

By exploiting the two different look directions, it is possible to estimate also the east-west component of the movement as part of the 2D drift estimate. It has been computed using a multi-scale cross-correlation approach of the geocoded data of the outward and inward flown passes. The input data were Gaussian filtered and resampled to a common 1m by 1m UTM grid. The estimated 2D displacement vectors were then transformed to ice drift velocity measurements using the exact time difference between the passes corresponding to the respective centres of the synthetic aperture. For outward /eastern areas the time difference is in the order of few tens of minutes, whereas it is almost 2 hours for the inward area/western part. Shifts of several hundred meters have been measured in some areas, meaning that sea ice areas might shift outside the image borders. Nevertheless, consistent measurements have been achieved in all frequencies and polarisations and even when combining different frequencies/polarisations in the cross-correlation operation. **Figure 4** presents the visualisation of the 2D drift velocity vectors for the above shown segments using as input X-band data in VV polarisation. The drift magnitude is color-coded and the direction and strength is indicated by the arrows. Grey areas indicate non-valid estimates, which occur either at ice discontinuity locations or where the ice flows have moved outside the swath. Land fast ice is shown in the left of segment 3, whereas the other segments show a similar trend as the ATI analysis.

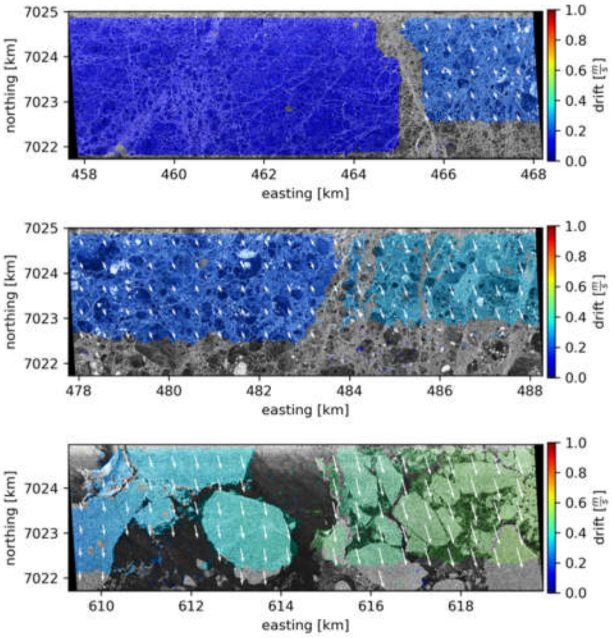

Figure 4 2D ice drift velocity maps derived from X-band cross-correlation of geocoded data of the two passes, corresponding to same segments 3,5 and 18.

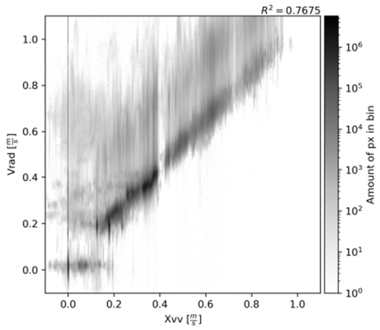

Figure 5 Similarity plot of the north-south component of ice drift, when derived from the cross-correlation (horizontal axis) vs. the measurement of radial velocity with ATI from the outward flown pass (vertical axis).

Figure 5 shows the similarity plot of the north-south ice drift component with measurements of radial velocity (projected to ground) from the ATI measurements. The scatter plot/2D histogram summarizes the measurements for the complete campaign, i.e. including all segments. ATI is sensitive to the instantaneous ice drift motion, whereas the 2D correlation relies on cumulative displacements and represents an average value. Assuming stable conditions (ice drift with constant velocity and direction), the two measurements are expected to give very similar values, which is indeed the case. The distribution of velocities is multi-modal and roughly 4 different ice drift regimes can be recognized.

4.2 Sea ice classification

The polarimetric measurements of the three used frequencies allow the computation of standard PolSAR image features such as polarimetric entropy, alpha angle, anisotropy (see e.g. [4]), as well as correlation between the different polarimetric channels. These features can then be used for visual interpretation as well as an input to unsupervised clustering or – if reference data is available – for supervised training of a classifier that maps the data to a semantic label. **Figure 6** shows the phase difference between HH and VV polarization in C-band of the same segments as above (i.e. the phase of the complex correlation coefficient γ, see Eq.2, where $\langle .,. \rangle$ denotes the scalar product and $(.)^*$ complex conjugation, respectively) and clearly illustrates the descriptive power of such features.

$$\gamma = \frac{\langle S_{HH}, S_{VV}^* \rangle}{\sqrt{\langle S_{HH}, S_{HH}^* \rangle \langle S_{VV}, S_{VV}^* \rangle}} \qquad (2)$$

→ flight direction (~east)

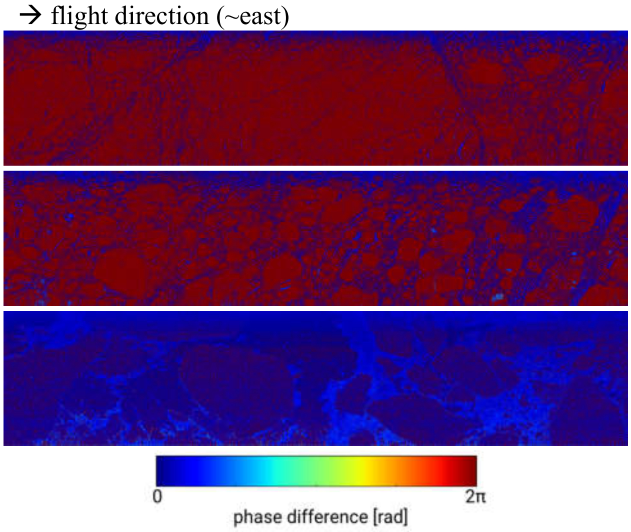

Figure 6 Phase difference between HH and VV in C-band for the same three segments as above.

Ice closer to the shore (first row) shows phase differences closer to 2π (small negative values), where channels and cracks can be clearly distinguished from the main ice mass. This effect is even more emphasized at a larger distance from the cost (second row), where individual parts of ice can clearly be distinguished. Ice furthest away from the cost (third row) shows mainly positive phase differences close to zero.

Due to the lack of proper reference data denoting different sea ice types present in the data, we perform unsupervised clustering. We apply k-Means with $k=10$ clusters using the Bartlett distance $d(A,B)$ between polarimetric variance-covariance matrices A,B, i.e.

$$d(A,B) = \frac{\log(|A+B|^2)}{|A| \cdot |B|} \qquad (3)$$

In order to cope with the large amount of data, we apply an iterative version of k-Means where cluster centres are optimized for n_1 iterations based on N samples of only one image after which the next image is loaded and the optimization continues. This process is repeated n_2 iterations over all images. The following results are obtained with $n_1 = n_2 = 5$ and $N=2M$. The optimization converged relatively fast and varying these parameters did not lead to significantly different results.

While the computation of the cluster centres is performed for each frequency band independently and is based on images acquired during the outward pass only, the found clusters are highly consistent between the different frequencies and also compared to the inward pass, i.e. similar scene elements are assigned to similar clusters. Furthermore, although a direct semantic interpretation of most clusters is not possible, the computed clusters represent image structures with clearly different textural and polarimetric properties. **Figure 7** shows three exemplary cluster assignments of a segment from the inward pass (i.e. a segment not used during cluster computation). The three clusters correspond to large, rather homogeneous segments (e.g. water and ice floes), lines and ridges (e.g. cracks), and small, nearly point-like structures (e.g. icebergs), respectively.

← flight direction (~west)

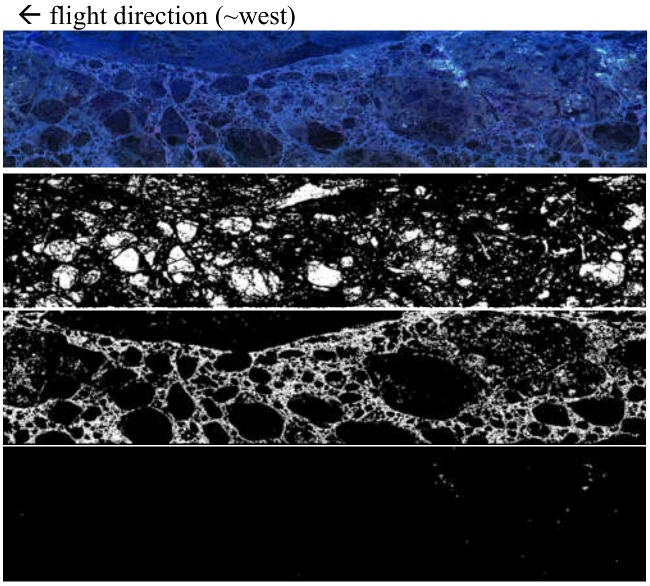

Figure 7 Three exemplary clusters based on the C-band image shown in the first row (same colour coding as in Fig.2)

Figure 8 shows the cluster likelihood of the polarimetric entropy and illustrates that individual clusters clearly represent different backscattering processes with different polarimetric properties.

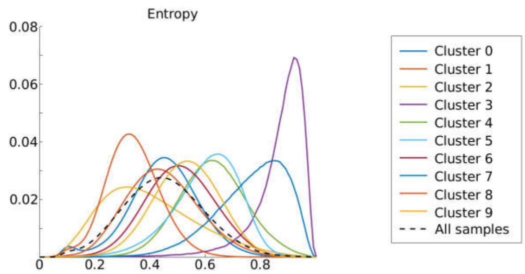

Figure 8 Cluster likelihood of the polarimetric entropy.

Since unsupervised clustering is employed, the clusters represent dominant polarimetric and textural image structures. A direct mapping of these clusters to specific semantic classes is not possible and would require a further step based on supervised learning exploiting task-specific reference data for training. Nevertheless, different semantic classes (such as water, smooth ice or snow cover, ice cracks and ridges, icebergs, etc.) cause certain textural and polarimetric signatures that are detected as unique structures by the clustering. These results show that at least some semantic classes can be distinguished based on the obtained PolSAR data. Future work can exploit above mentioned features and/or the clustering itself together with available reference data provided by sea ice experts to automatically classify sea ice according to different categories such as age, thickness, etc. The consistency and robustness of the clustering indicates that a corresponding classifier might be able to generalize well, at least over different segments of the same flight or multiple flights over the same area.

5 Acknowledgement

The authors acknowledge the support of the Canadian Ice Service, which provided the up-to-date ice charts for campaign planning. This work is performed under ESA-ESTEC contract no. 4000128351/19/NL/FF/gp.

6 Literature

[1] P. Lopez Dekker, H. Rott, P. Prats-Iraola, B. Chapron, K. Scipal, E. De Witte: "HARMONY: An Earth Explorer 10 Mission to Observe Land, Ice, and Ocean Surface Dynamics", Proc, IGARSS 2019.

[2] R. Horn, M. Jaeger, M. Limbach, A. Nottensteiner, M. Pardini, A. Reigber, R. Scheiber „F-SAR – Recent Upgrades and Campaign Activities", Proc. International Radar Symposium IRS, 2017.

[3] M. Jäger, R. Scheiber, and A. Reigber, "Robust, model-based external calibration of multi-channel SAR sensors using range compressed raw data," Remote Sensing, 2019, 11(22), 2674.

[4] J.-S. Lee and E. Pottier, "Polarimetric Radar Imaging – From Basics to Applications", CRC Press, 2009.